Microstrip plastic scintillating detector system for quality assurance in synchrotron microbeam radiotherapy

F. Thevenet, S. Keshmiri, J. Degouttes, J. Livingstone, G -N. Lu, J -F. Adam, P. Pittet

▶ **To cite this version:**

F. Thevenet, S. Keshmiri, J. Degouttes, J. Livingstone, G -N. Lu, et al.. Microstrip plastic scintillating detector system for quality assurance in synchrotron microbeam radiotherapy. Scientific Reports, 2025, 15 (1), pp.277. 10.1038/s41598-024-80736-0 . hal-04862419

HAL Id: hal-04862419
https://hal.science/hal-04862419v1

Submitted on 3 Jan 2025

HAL is a multi-disciplinary open access archive for the deposit and dissemination of scientific research documents, whether they are published or not. The documents may come from teaching and research institutions in France or abroad, or from public or private research centers.

L'archive ouverte pluridisciplinaire **HAL**, est destinée au dépôt et à la diffusion de documents scientifiques de niveau recherche, publiés ou non, émanant des établissements d'enseignement et de recherche français ou étrangers, des laboratoires publics ou privés.

Distributed under a Creative Commons Attribution - NonCommercial - NoDerivatives 4.0 International License

scientific reports

Check for updates

OPEN

Microstrip plastic scintillating detector system for quality assurance in synchrotron microbeam radiotherapy

F. Thevenet[1], S. Keshmiri[2], J. Degouttes[1], J. Livingstone[4], G -N. Lu[1], J -F. Adam[2,3] & P. Pittet[1,5]✉

Synchrotron microbeam radiotherapy (MRT), which has entered the clinical transfer phase, requires the development of appropriate quality assurance (QA) tools due to very high dose rates and spatial hyperfractionation. A microstrip plastic scintillating detector system with associated modules was proposed in the context of real-time MRT QA. A prototype of such a system with 105 scintillating microstrips was developed and tested under MRT conditions. The signal obtained from each microstrip when irradiated was reproducible, linear with the dose, and independent of both the dose rate and the beam energy. The detector prototype was capable of measuring an entire 52-microbeam field in real time and exhibited outstanding radiation hardness. It could withstand more than 100 kGy absorbed dose, which is at least ten times higher than the doses reported in the literature for plastic scintillators before deterioration. The potential of this detector system in MRT QA was demonstrated in this study.

Keywords Dosimetry, Plastic scintillators, Microbeam Radiotherapy, Quality assurance

Synchrotron X-ray microbeam radiotherapy (MRT) is an external beam radiotherapy modality that features highly coherent X-rays to deliver treatments at high dose rates (up to a few kGy/s) with spatial hyperfractionation through arrays of microbeams (typically 50 μm wide beams, separated by 400 μm). In this way, MRT takes advantage of both FLASH and dose-volume effects[1–3]. MRT translational research has been ongoing in synchrotron facilities through veterinary trials[4], which will enable the clinical transfer of this promising technique. In that respect, the development of state-of-the-art commissioning and patient-specific quality assurance (QA) is required[5,6]. This requires real-time dosimeters with high spatial resolution and sufficient radiation hardness. Moreover, a wide dynamic range and low energy dependence of the detector response are also needed to measure the peak-to-valley dose ratio (PVDR), a well-established dose index for MRT[7]. It is worth mentioning that the energy dependence of detectors is a particular issue in MRT, which uses X-ray beams in the orthovoltage domain with a much lower average energy (i.e., approximately 100–120 keV) than those used in conventional external beam radiotherapy.

Different technologies have been proposed for MRT dosimetry. Radiochromic films are suitable for commissioning procedures with sufficient spatial resolution for individual microbeam measurements[8,9], however, they have limitations for day-to-day QA, including off-line-readout with insufficient dynamic range. Silicon strip detectors have been proposed in either a single strip version or in array form for simultaneous peak and valley dose measurements[10–12]. MOSFET have also been studied for MRT Dosimetry[13]. The main disadvantages of silicon-based detectors (including strip and MOSFET[14]detectors) are the lack of tissue equivalence for low to medium energy x-rays (such as the one used in MRT). Another issue for MOSFET detectors in particular is that the readout signal and lifetime is related to the accumulated dose[14]and requires regular calibration and replacement. A diamond-based detector has also been proposed for online beam monitoring and portal dosimetry[15]. Single-chip single-crystal diamond detectors can also be used for absolute dosimetry and QA if their dimensions permit adequate spatial resolution (1–3micrometers thick)[16]. Diamond exhibits a better tissue

[1]Universite Claude Bernard Lyon 1, INL, UMR5270, CNRS, INSA Lyon, Ecole Centrale de Lyon, CPE Lyon, 69622 Villeurbanne, France. [2]Univ. Grenoble Alpes, INSERM, UA07 STROBE, 2280 rue de la piscine, 38400 Saint-Martin d'Hères, France. [3]Centre Hospitalier Universitaire Grenoble Alpes CHU-GA, Grenoble 38043, France. [4]Univ. Grenoble Alpes, CNRS, Grenoble INP*, LPSC-IN2P3, 38000 Grenoble, France. [5]Institute of Engineering Univ. Grenoble Alpes, Grenoble, France. ✉email: patrick.pittet@univ-lyon1.fr

equivalence than silicon-based detectors, however, its mass density remains high compared to that of soft tissue, which could raise a problem of detector response for MRT QA.

Real-time, non-semiconductor detectors, such as plastic-scintillator-based detectors (with coupled fibers and photodetectors) have also been proposed for FLASH therapy and MRT dosimetry[17–19]. One example of such a detector system makes use of a 10 μmthick film of plastic scintillator optically coupled to a an optical fiber with a core 1 mm in diameter[17]. Archer *et al.*[17] obtained a 1D profile of an MRT microbeam array with a spatial resolution of 10 μmby scanning the plastic scintillator horizontally in the beam. The same authors[18] also used the detector to measure depth-dose curves, demonstrating the tissue equivalence of plastic scintillator detectors. Using such a detector for MRT QA, however, is time-consuming as strict detector alignment procedures and scanning of the radiation field are required. It is noteworthy that any misalignment significantly reduces spatial resolution due to the high aspect ratio of the scintillating disc.

The aim of this study was to fabricate and test a new multichannel plastic scintillator detector system specifically for MRT QA.

Materials and methods

The proposed detector system is depicted in Figure 1. It consists of:

- a microstrip plastic scintillating detector with a multi-channel optical guide output,
- a coupled photodetection module based on a CMOS linear sensor with readout electronics.

The scintillating detector was built with two distinct materials to form optical guides: 1) BC-408 for the scintillating core, and 2) Cyclic Olefin Copolymer (COC) for the non-scintillating core[20,21]. UV-cured acrylic urethane (an organic material) was used for optical cladding[22,23]. The main properties of these materials are summarized in Table 1. These materials were chosen for their tissue-equivalence: their density and atomic number were close to those of soft tissue and solid water phantom materials. No significant change was expected in the dose distribution or charged particle equilibrium (CPE) in the microstrip detector when compared to the surrounding materials.

For the prototype instrumentation, the photodetection module is a CMOS linear sensor (S11639-01 Hamamatsu Photonics K.K, Japan) with 2048 vertical pixels (14 μm × 200 μm), coupled to the output of the microstrip plastic scintillating detector. This CMOS sensor implements on-chip charge pre-amplification and is driven by a laptop via an interface board (C13015-01, Hamamatsu Photonics K.K, Japan) which performs 16-bit data acquisition of the analog video signal.

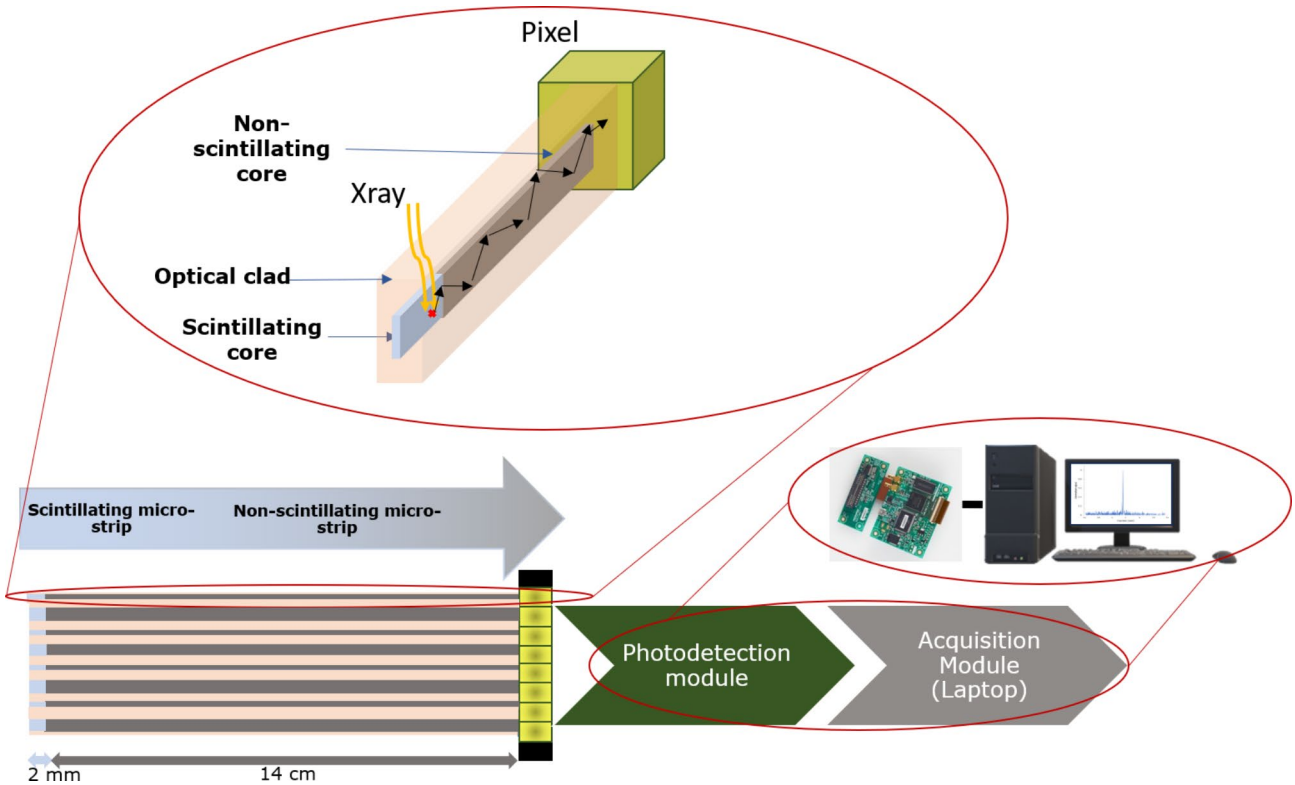

Fig. 1. The microstrip plastic scintillating detector system developed in this study. The zoom on the left shows the 2 mm long scintillating section in light grey and the 14 cm long non-scintillating section in dark grey. The zoom on the right shows the photodetection module based on a CMOS linear image sensor with 2048 14 μm wide pixels.

Material	Tissue, Soft (ICRU-44)[24]	Tissue-equivalent plastic (RW3) (LAP GmbH Laser Applikationen, Germany)	BC-408 (Luxium Solutions, USA)	Cyclic Olefin Copolymer(COC)	Acrylated urethane (AA3311, Henkel AG, Germany)	PMMA
Role	Reference	Phantom	Scintillating Core	Non-scintillating Core	Optical clad	Buffer material
Density ($g.cm^{-3}$)	1.060	1.045	1.032	1.020	1.1013	1.190
Relative Electron density	1.000	1.012	0.958	1.003	0.895	1.159
Mean Excitation Energy (eV)	72.3	67.1	64.7	60.2	74.5	74.0
$(Z/A)_{eff}$	0.549	0.536	0.541	0.557	0.497	0.540
Refractive index @589 nm	-	-	1.580	1.533	1.500	1.491

Table 1. Physical properties relevant to X-ray interactions with matter and dosimetry for soft tissue, liquid water, and the materials used in the integrated multi-channel plastic scintillating module.

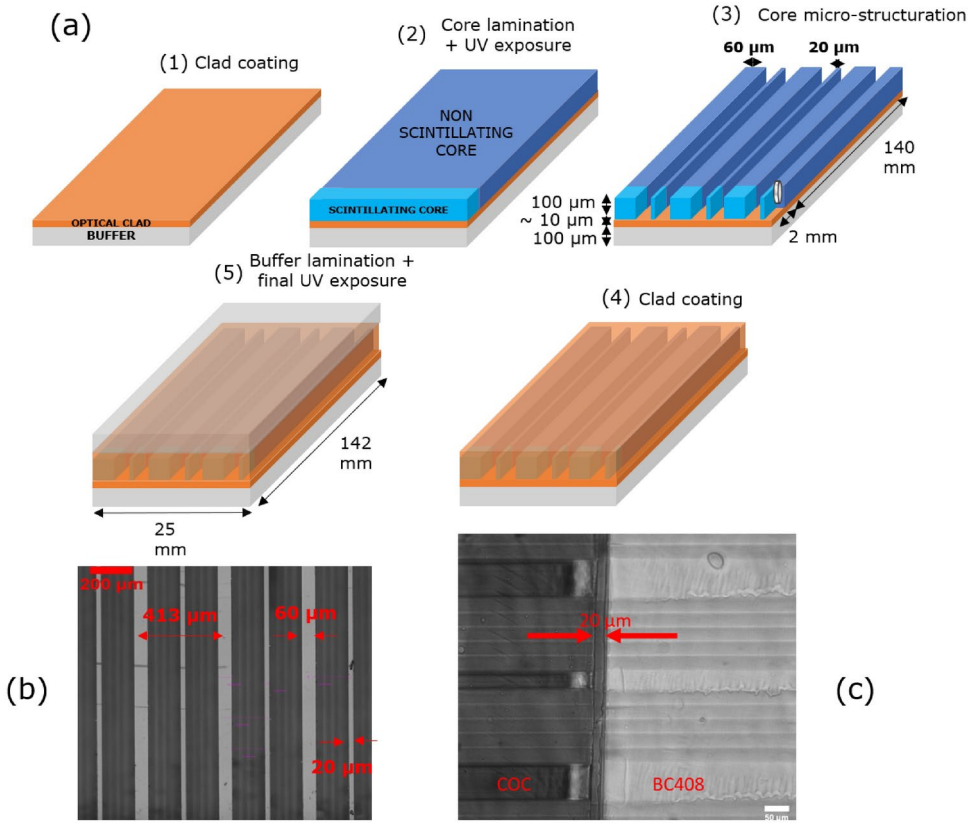

Fig. 2. (**a**) Main steps of the microstrip plastic scintillating detector manufacturing process, (**b**) Microscopic views from above the microstrip detector after the third step of micro-structuring, (**c**) Microscopic view of the scintillating/non-scintillating interface of the microstrip detector. This process was developed using the clean room facilities of Institut des Nanotechnologies de Lyon (INL) and the Nanolyon platform.

Design and fabrication of the microstrip plastic scintillating detector

Considering the 413 µm microbeam pitch measured at the MRT treatment isocenter, the plastic scintillating detector was designed with alternating 20 µm and 60 µm wide microstrips (100 µm height) with a 206.5 µm pitch for simultaneous peak and valley dose measurements. The narrowest strips were of interest for high dose measurements (peaks), while the wider strips enabled the measurement of much lower valley doses.

The sensitive area of the detector was 24 mm wide (with 105 microstrips), which covered the width (20 mm) of the field typically used for reference dosimetry[25]. The sensitive volumes (2 mm long, 0.1 mm thick scintillating cores) were located 14 cm below the photodetection module to collect data at a distance from scatter generation. The 2 mm length was sufficient to collect the irradiation signal regardless of the beam height used for the irradiations (a maximum height of 0.795 mm was possible at the ID17 beamline of the European Synchrotron, ESRF). A test structure with 142 mm length scintillating cores was also developed to measure losses in optical guides.

Figure 2 shows the main steps of the fabrication process for the microstrip plastic scintillating detector:

1. A clean 100 μm-thick foil of PMMA was coated with a thin layer of UV-curable optical cladding.
2. A 100 μm-thick BC-408 foil and a 100 μm-thick Cyclic Olefin Copolymer (COC) foil were placed in contact with each other on this cladding layer. The residual gap between these foils was kept as small as possible and checked using a microscope.
3. This assembly was laminated using a hot roll laminator at 120°C with a speed of 0.9 m/min (SKY-335R6, General Cover, France) and then UV-cured for 15 s at 64 mW/cmÂ² (UV-KUB2, KLOE, France).
4. The BC-408 and COC layers were micro-structured into 20 and 60 μm wide strips with a pitch of 206.5 μm using a dicing saw (DAD3220, DISCO Corp., Japan) equipped with a diamond blade (ZH05-SD1700-N1-50, DISCO Corp., Japan). The kerf width was 45 μm.
5. The top of the micro-structured stack was covered with a thin layer of UV-cured optical cladding and overlaid with a 100 μm-thick PMMA foil. The final assembly was laminated on a hot roller laminator at 70°C with a speed of 0.9 m/min, then UV-cured for 15 s at 64 mW/cm^2.

It is noted that the scintillating and non-scintillating foils were assembled upstream of the guide microstructuring step, which implied an inherent self-alignment between the scintillating and non-scintillating microstrips, as shown in Figure 2c. In addition, the gap between these aligned microstrips, which was a few tens of micrometers, was filled by the optical cladding (during step 5 of the process), which acted as an index-matching material. In this way, a good quality of optical coupling was obtained between the scintillating and clear sections of each microstrip.

Prototype testing

The fabricated prototype was first tested using UV sources and then characterized under synchrotron-generated X-rays from the ID17 biomedical beamline of te European Synchrotron (ESRF) in Grenoble, France.

UV testing

UV tests aimed to check for light signal emission and transmission from the scintillator to the CMOS sensor, as well as crosstalk between adjacent channels. Firstly ("transmission test"), the entire scintillating area of the prototype was exposed to a 375 nm UV lamp (NU-8-KL, Benda GmbH, Germany) to check signal transmission between scintillator microstrips and optical guides. A sCMOS camera (Zyla 5.5, Andor-Oxford Instruments Ltd, UK) was used to acquire images of the output of the optical guides. Secondly ("crosstalk test"), a single strip of the scintillating area was exposed to a fiber-coupled UV LED with the setup shown in figure 3a) to estimate

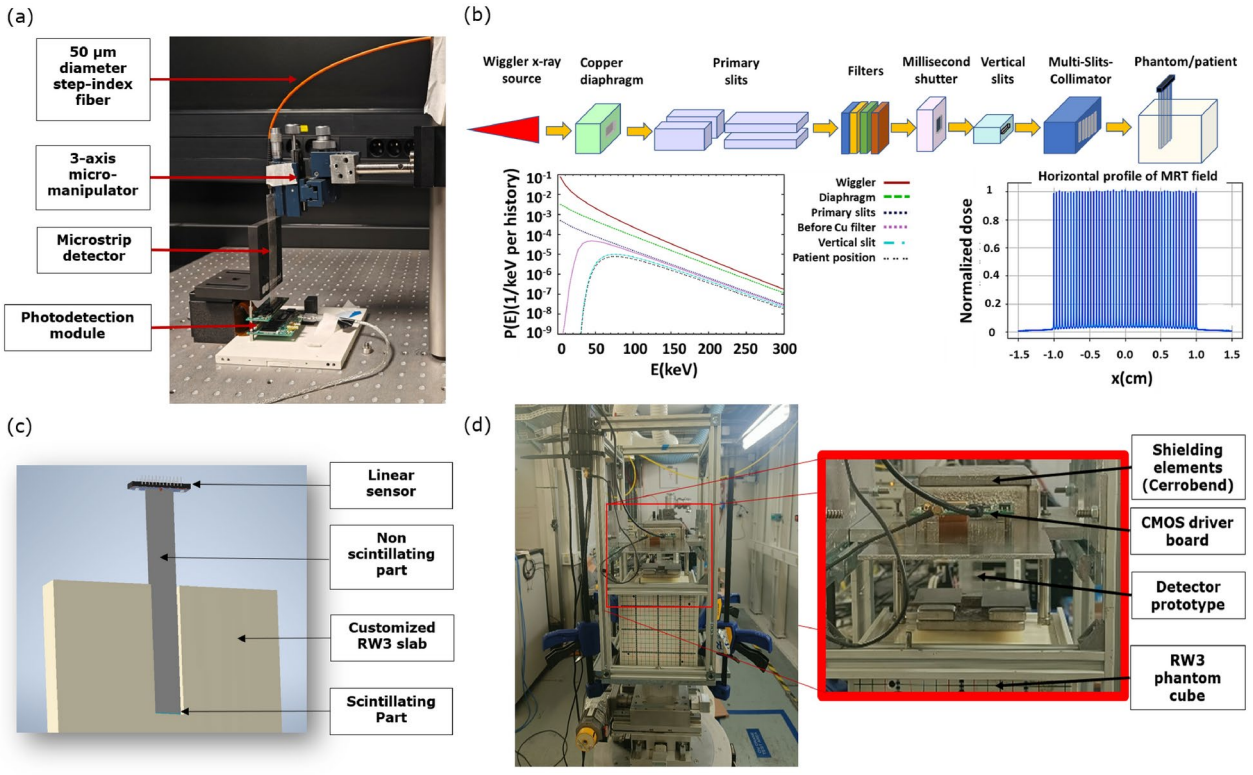

Fig. 3. (**a**) Lab testing setup using a 310 nm LED coupled to a 50 μm fiber for single microstrip excitation. (**b**) Schematic view of the ID17 beamline with the different beam modifiers and associated beam profiles[26,27]. (**c**) Schematic view of the customized RW3 slab adapted for holding the microstrip plastic scintillating detector. (**d**) Photos of the full setup in MRT QA conditions at the ESRF ID17 beamline with a zoom on the detection system shielded by a Cerrobend box.

optical crosstalk. A 310 nm filtered LED light source (FFC-0310-000, Mightex Systems, USA) was coupled to a 50 μm diameter step-index fiber. The distal end of this fiber was attached to a 3-axis micro-manipulator for precise positioning of the UV spot on the detector. The detector output was coupled to the photodetection module by means of a micro-fabricated COC window of the same size as the sensor, with a central 500 μm notch for the detector to pass through, then sealed with UV glue. Finally ("transmission loss test"), to evaluate signal transmission losses in a 60 μm scintillator strip, the 142-mm-long test structure was exposed to the spot from the fiber-coupled UV LED. Its output was coupled to the CMOS sensor. The spot position on the strip was controllable to modify the transmission length of the scintillator strip. The losses were characterized at the scintillating signal wavelength (418 nm).

MRT testing

Irradiation tests were carried out at ID17, in the MRT hutch. A schematic view of the main beamline components is represented in Figure 3b). A low-divergence filtered white beam (ranging from 50 to 500 keV, with an average energy of 121 keV) was used. The white beam in the case of ID17 refers to the broad energy spectrum of X-rays produced by the wiggler source. The white beam passed through a copper diaphragm with a rectangular aperture of 24 mm x 1.5 mm. This beam was then collimated by primary slits and filtered through a series of carbon, aluminum, and copper filters to reduce low-energy components. The filtered beam was collimated vertically by a set of upstream tungsten blades to define its height. Fixed beam heights of 0.051 mm, 0.1 mm, 0.52 mm or 0.795 mm are available, but the beam height was fixed at 0.52 mm for the entirety of this study. Spatial fractionation of the beam was performed using a high-precision tungsten carbide multi-slit collimator (MSC) with a nominal slit width of 50 μm and an inter-slit distance of 400 μm[26,28]. This process produced a radiation field of 20 mm x 0.52 mm containing 52 microbeams of 50 μm width, equally spaced with a 413 μmpitch at the treatment isocenter, which was located at a distance of 1.5 m from the MSC. PMMA slabs ranging from 0.5 to 32 cm thick could be placed before the multi-slit collimator to adjust the peak dose rate in the microbeam from approximately 4 kGy/s down to approximately 0.4 kGy/s. These peak dose rates were about 75% of the dose rates measured using a pinpoint ionization chamber placed at 2 cm depth in the phantom and irradiated with a 2 cm by 2 cm broad beam (as proposed by Fournier et al. by adapting the IAEA TRS 398 code of practice[25]).

The microstrip plastic scintillating detector was inserted in a customized RW3 (PTW, Germany) slab, as illustrated in Figure 3c), and positioned at 2 cm depth in a 18 cm x 18 cm x 18 cm RW3 phantom, as shown in Figure 3d). The linear image sensor and associated electronics were shielded from irradiation by using the Cerrobend box shown in Figure 3d).

To achieve precise alignment of the microbeams on the detector, a systematic centering process was implemented by using the remote controlled lateral and vertical motorized sample translation stages (mounted on the Kappa-type Goniometer irradiation stage)[29]. These translation stages were used for positioning the treatment isocenter in the microbeam field in MRT preclinical and veterinary trials[30]. The alignment process consisted in translating the phantom (which incorporates the detector) and monitoring the scintillating signal from the detector, when irradiating in step and shoot mode (1 s irradiations). Coarse steps of 50 μm were first used to find the approximate area of maximum signal on the 60 μm-wide microstrips of the detector. Once the maximum signal area was identified, finer steps of 5 μm were used for a finer alignment of the microbeams on the detector sensitive volumes.

The measurements were performed using one-second long static exposures, which corresponded approximately to a 4 kGy peak absorbed dose at the sensitive volume level. The integration time of the photodetection module was set to 100 ms. This configuration allowed for the acquisition of 10 frames per irradiation. It should be noted that these static exposure tests did not mimic the dynamic conditions of an actual treatment setup, where the RW3 phantom (or patient) would be continuously moved through the field at a constant speed to cover the whole target, as described by Ocadiz *et al.*[31]. However, these tests served as a first approach to evaluate the response of the detector under controlled conditions.

Finally, the beam was collimated down to a single microbeam to study the repeatability of the response of each individual microstrip to irradiation. The repeatability index was defined as the standard deviation measured over 30 frame acquisitions from 3 one-second exposures (10 frames acquired per exposure).

Results and discussion

UV testing

Figure 4a) shows an acquired image from the transmission test. The microstrip signals are clearly observable above the background noise. This confirmed that the COC cores exhibited excellent performance for the optical guidance of the UV-induced blue emission from BC-408 regardless of the microstrip scintillators width. The FWHM of the peaks was measured at 16 ± 4 μm and 85 ± 4 μm for the 20 μm and 60 μm wide microstrips, respectively (Figure 4b).

Furthermore, when considering each strip signal (area under the curve for each peak in Figure 4b), it was observed that the signal at the output of the 20 μm wide microstrips was around ten times weaker than that at the output of the 60 μm wide microstrips. This observation was in line with the analysis published by Shi *et al.*[32], which concluded that narrower waveguides experienced greater light scattering due to a higher proportion of modal power overlap. Narrower microstrips confined more of the modal power to the waveguide boundaries, which increased scattering losses due to material and surface imperfections, whereas larger microstrips allowed the modal power to spread out more, reducing the light interactions with the boundaries and the scattering losses.

Figures 4c) and 4d) show acquired signals from the crosstalk test. The estimated crosstalk depends on the width of the strip exposed: for a 60 μm strip (Figure 4c), each adjacent 20 μm channel received less than 2.7% of the 60 μm strip signal, and for the 20 μm strip (Figure 4d), each adjacent 60 μm channel collected up to 23%

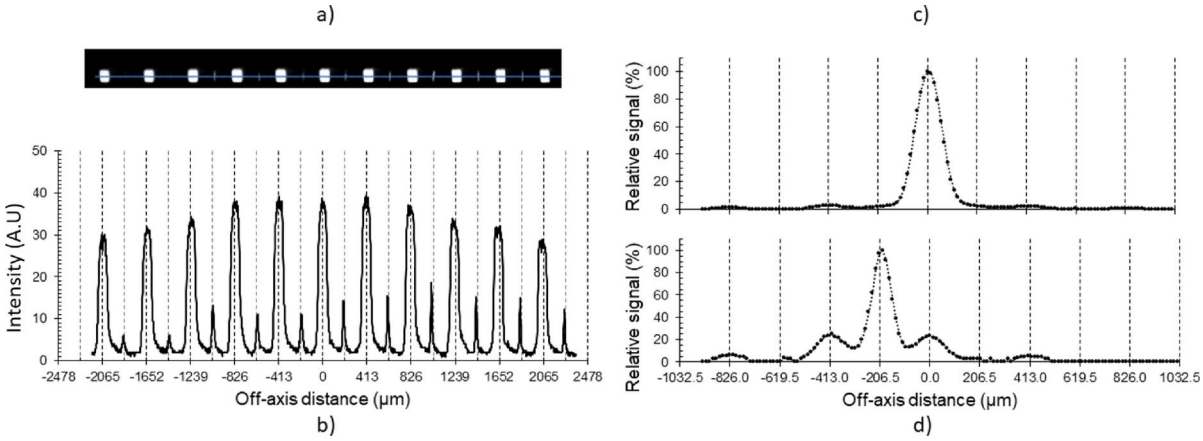

Fig. 4. (**a**) sCMOS camera image of the scintillation signal obtained after UV excitation of the detector; (**b**) 1D intensity profile of this scintillation signal (in arbitrary units) along the blue line displayed in a); (**c**) signals measured using the photodetection module during UV excitation for a single 60 μm wide microstrip and (**d**) a single 20 μm wide microstrip.

of the signal from the exposed 20 μm strip. This optical crosstalk was too high, in particular in case of 20 μm -wide microstrips. Typically, for simultaneous peak and valley dose measurements in MRT, the Peak to Valley Dose Ratio varies from 1% to 10% (depending on the irradiation mode and on the considered depth). This made us focus on peak measurements using the 60 μm-wide microstrips.

Transmission loss in the 60 μm scintillation microstrip was measured (transmission loss test) and evaluated at about 2.7 dB/cm. This loss was mainly due to the surface roughness of the core sidewalls, with a ∼50 nm root mean square roughness value, as measured on atomic force microscope images of the prototypes (data not shown). This sidewall roughness resulted from the dicing step in the micro-structuring process. The top and bottom surfaces of the BC-408 and COC foils were glass-quality polished[32]. To reduce these losses, a solvent vapor treatment of the microstructured COC cores was tested[33], which reduced the wall surface roughness value to less than 5 nm and gave optical quality to the surface of the core walls.

MRT testing

The prototype was also tested in MRT conditions with a CMOS sensor to acquire microstrip signals for a 1s exposure (100 ms integration time) of the detector with a 20 mm microbeam array (52 equally spaced microbeams). The results are presented in Figure 5a). It should be noted that the presented data are raw data, without any calibration performed to equalize the channels. Indeed, as shown in Figure 5a), the microbeams should have had a uniform intensity across the whole array. The variation in signal response between each microstrip might have been due to the micro-fabrication process leading to (i) variable roughness from one strip to another, (ii) a variable gap between the scintillating material and the non-scintillating guides (see Figure 2c), and (iii) a difference between the microbeam (and microstrip) pitch (413 μm) and the pixel size (14 μm) of the linear sensor, leading to some variable edge effects. A reliable calibration could be performed using a PTW microDiamond detector scan on the same field[16]or Gafchromic film[31] measurements. Although this type of calibration could not be performed during the current study, it is planned for future system optimizations.

A 25% background noise was observed (SNR = 4) when exposing the system with a 20 mm wide microbeam array. This noise was a combination of crosstalk effects and x-ray scatter detection on the linear camera (Figure 5a). When using dynamic MRT irradiation to cover vertically extended fields, this background noise became prohibitive for MRT-QA as it exceeded the signal. To address this issue, two main improvements were focused on: (i) reducing the optical losses of the microstrip plastic scintillating detector (see previous section) and (ii) minimizing the indirect irradiation of the linear camera by optimizing the shielding and the distance from the irradiation field. The dicing saw used for the microstrip fabrication, which currently exhibits a 145 mm maximal dicing limitation, could be upgraded to increase the prototype length.

The average signal normalized to the maximum intensity recorded on the CMOS sensor for a single microbeam 1s exposure is shown in Figure 5b). This demonstrated the potential of the detector to detect a single microbeam with a signal-to-noise ratio of approximately 10. The signal observed 413 μm to the left was likely to be a real signal corresponding to some imperfections when collimating the beam down to one single microbeam by using the primary slits that were located in the tunnel, close from the wiggler, more than 30m upstream of the multi-slit collimator. This had already been observed by Di Franco *et al.*[15] with a stripped diamond detector used for portal dosimetry and with HDV2 Gafchromic films, as shown in Figure 5d. This signal delivered a dose about 30% lower than the dose delivered by the main microbeam up to about 200 μm on the left of the peak. Our prototype was able to detect this phenomenon with an SNR of 3, on the adjacent 60 μm-wide microstrip which was located 413 μm to the left. This can probably be explained as follows (assumption that remains to be verified): some of the UV photons emitted by the BC-408 primary fluors in the 20 μm-wide intermediate strip (which is irradiated in this configuration) escaped the strip[34] and excited the wavelength shifters in its adjacent 60 μm wide strips. It is noted that this satellite signal could be removed by using a "backup" slit placed

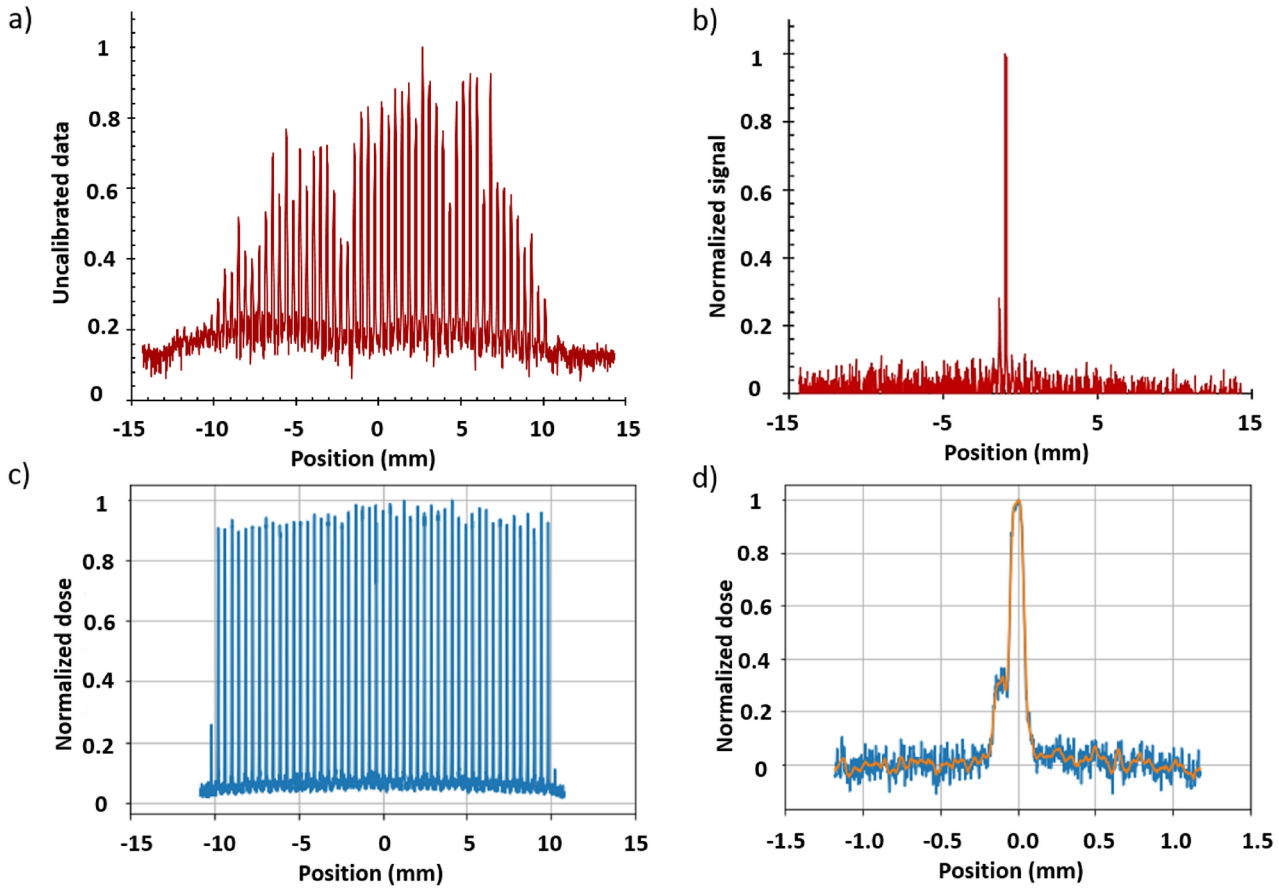

Fig. 5. Signal recorded at the detector system output for (**a**) irradiation with a 20 mm microbeam array (52 microbeams) and (**b**) a single microbeam irradiation. The measurements were performed at a 2 cm depth in water in a solid water phantom. The corresponding radiation field profiles as measured by Gafchromic films are shown in **c** and **d**, respectively[15]..

downstream of the multi-slit collimator instead of using the primary slits as the only beam collimation device. Moreover, the repeatability of the measurements was found to be better than 1% ($\pm 1\ \sigma$) as measured with 30 consecutive exposures.

In an another test, the detector was translated by 206.5 μm to align the 20 μm strips with the microbeams. No signal was detected, which is unlikely to be explained solely by the reduced photon and secondary electron interaction in the 20 μm wide microstrips compared to the 60 μm wide microstrips. Leutz *et al.*[34]pointed out serious issues when miniaturizing high-yield plastic scintillating materials compared to low-yield plastic scintillating materials. High-yield plastic scintillating materials are three-component scintillators[35], where the UV photons emitted by the primary fluor should be absorbed by wavelength-shifters in their vicinity to form the light signal. When miniaturized too much, due to the very low concentration of wavelength shifter, the probability of the UV photons either being self-absorbed or escaping from the BC-408 material before reaching the wavelength shifter becomes too high. Low-yield plastic scintillating materials are one-component scintillators[34]and might be more appropriate for our purpose but are no longer manufactured. One idea would be to propose custom-designed low-yield plastic materials or to develop other sensitive volumes based on quantum dots[36].

Figure 6shows that the response of the detector system was linear with the dose rate without energy dependence within the energy interval covered in this study. This means that the detection system, when operating in integration mode, had a linear response with the absorbed dose independently of the dose rate in the 0.4 to 4 kGy/s range. It is important to mention that, at the end of this test, a cumulative dose of over 100 kGy was deposited in the detector over 1.5 minutes (each 1s exposure was separated from the next by a 5 s pause without radiation to change the attenuator configuration). The radiation hardness of the detector was more than an order of magnitude higher than that reported in the literature for plastic scintillators[35,38,39]. This result was attributed to the specificities of the MRT irradiation conditions used in our research:

- Plastic scintillators experienced two types of degradation: transmittance degradation and light yield degradation, with transmittance degradation being more linked to the absorbed dose than light yield degradation[35]. Furthermore, the COC used for the optical guide core in the microstrip detector could withstand a gamma sterilization dose of 200 kGy without any noticeable change in its absorbance and transmittance in the visible

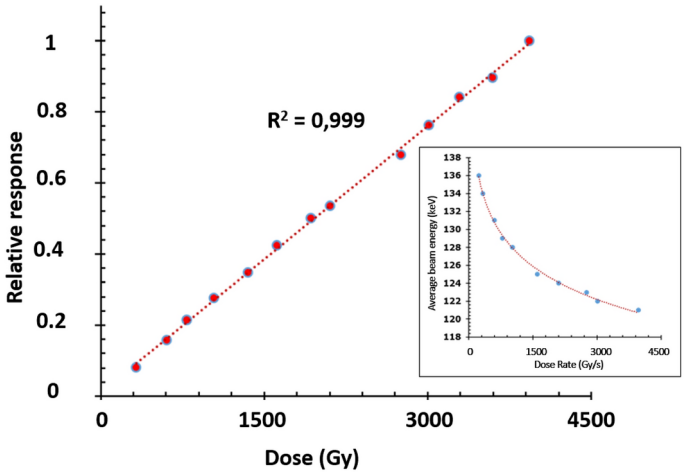

Fig. 6. Detector system response recorded for a single microbeam as a function of peak dose for the 1-second exposure time. Each point in the plot corresponds to the average response over 10 frames normalized to the maximum value at the highest dose. The error bars represent the standard deviation and are not visible in the plot as they are smaller than the symbols. The peak dose rate was reduced by inserting PMMA plates as an absorbing medium. The average energy of the beam, obtained from the spectra calculated using the Oasys software[37] is represented in the insert as a function of the peak dose rate to show the effect of beam hardening occurring when increasing the PMMA thickness to lower the dose rate.

Microstrip plastic scintillating detector	
Number of microstrips	105 channels
Pitch	206.5 µm
Cross-sections	20 µmx100µmand60 µmx100 µm(interleaved)
Scintillating lenght	2 mm
Non scintillating lenght	140 mm
Scattering losses	≈3 dB/cm
Numerical aperture mismatch loss	4 dB
Radiation hardness	> 100 kGy
Photodetection module	
Number of pixels	2048
Pixel size	14 µmx200 µm
Effective photosensitive area lenght	28.672 mm
Sensitivity	1300 V/(lx.s)
Analog to digital converter	16 bits
Detection system	
Repeatability	1%(1σ)
Dose reponse linearity	R2 =0,999 over [400-5400Gy] with no dose rate dependence

Table 2. Main characteristics of the proposed system.

spectrum[40]. Using a small (2 mm) scintillating module and a large (140 mm) COC clear guide contributed to avoiding transmittance degradation effects.
- MRT irradiations operated in the FLASH effect dose rate ranges, where radiation damage of the organic scintillator is lower for a given dose[35,41].
- The lower dose in the microbeam peak compared to that in a 20 mm wide open field[42,43] due to reduced scattering.Table 2 provides a summary of the main characteristics of our system prototype.

Conclusion

A detector system for MRT QA has been proposed. It is based on a plastic scintillator structured in microstrips, with optical guides and a photodetection module for signal acquisition. A 105-microstrip prototype was designed, fabricated and tested. MRT tests exhibited a linear dose response, dose rate independence and sufficient radiation hardness. Such a system could be routinely used in MRT QA. Further studies are underway

to improve the performance of the system. One such study aims to reduce losses in optical guides and increase the signal-to-noise ratio for use in dynamic MRT mode. These developments are the first step towards an instrumented phantom which would be of particular importance for patient-specific MRT QA as commonly used in conventional radiotherapy.

Data availability

Data is provided within the manuscript.

Received: 17 July 2024; Accepted: 21 November 2024
Published online: 02 January 2025

References

1. Zeman, W., Curtis, H. J. & Baker, C. P. Histopathologic Effect of High-Energy-Particle Microbeams on the Visual Cortex of the Mouse Brain. *Radiation Research* **15**, 496–514, https://doi.org/10.2307/3571293 (1961). Publisher: Radiation Research Society.
2. Favaudon, V. et al. Ultrahigh dose-rate FLASH irradiation increases the differential response between normal and tumor tissue in mice. *Science Translational Medicine* **6**, 245ra93–245ra93, https://doi.org/10.1126/scitranslmed.3008973 (2014). Publisher: American Association for the Advancement of Science.
3. Vozenin, M.-C. et al. The Advantage of FLASH Radiotherapy Confirmed in Mini-pig and Cat-cancer Patients. *Clinical Cancer Research* **25**, 35–42, https://doi.org/10.1158/1078-0432.CCR-17-3375 (2019). WOS:000455001100007.
4. Adam, J.-F. et al. Toward Neuro-Oncologic Clinical Trials of High-Dose-Rate Synchrotron Microbeam Radiation Therapy: First Treatment of a Spontaneous Canine Brain Tumor. *International Journal of Radiation Oncology*Biology*Physics* **113**, 967–973, https://doi.org/10.1016/j.ijrobp.2022.04.022 (2022).
5. Ashraf, M. R. et al. Dosimetry for flash radiotherapy: A review of tools and the role of radioluminescence and cherenkov emission. *Frontiers in Physics* **8**, https://doi.org/10.3389/fphy.2020.00328 (2020).
6. Siddique, S., Ruda, H. E. & Chow, J. C. L. Flash radiotherapy and the use of radiation dosimeters. *Cancers* **15**, https://doi.org/10.3390/cancers15153883 (2023).
7. Bräuer-Krisch, E. et al. Medical physics aspects of the synchrotron radiation therapies: Microbeam radiation therapy (MRT) and synchrotron stereotactic radiotherapy (SSRT). *Physica Medica* **31**, 568–583. https://doi.org/10.1016/j.ejmp.2015.04.016 (2015).
8. Ocadiz, A. et al. Film dosimetry studies for patient specific quality assurance in microbeam radiation therapy. *Physica Medica* **65**, 227–237. https://doi.org/10.1016/j.ejmp.2019.09.071 (2019).
9. Pellicioli, P., Bartzsch, S., Donzelli, M., Krisch, M. & Bräuer-Krisch, E. High resolution radiochromic film dosimetry: Comparison of a microdensitometer and an optical microscope. *Physica Medica* **65**, 106–113. https://doi.org/10.1016/j.ejmp.2019.08.012 (2019).
10. Davis, J. A. et al. Characterisation and evaluation of a pnp strip detector for synchrotron microbeam radiation therapy. *Biomedical Physics 'I &' Engineering Express* **4**, 044002. https://doi.org/10.1088/2057-1976/aab10c (2018).
11. Lerch, M. L. F. et al. New 3d silicon detectors for dosimetry in microbeam radiation therapy. *Journal of Physics: Conference Series* **777**, 012009. https://doi.org/10.1088/1742-6596/777/1/012009 (2017).
12. Davis, J. et al. Evaluation of silicon strip detectors in transmission mode for online beam monitoring in microbeam radiation therapy at the Australian Synchrotron. *Journal of Synchrotron Radiation* **29**, 125–137. https://doi.org/10.1107/S1600577521011140 (2022).
13. Rosenfeld, A. et al. Mosfet dosimetry of an x-ray microbeam. *IEEE Transactions on Nuclear Science* **46**, 1774–1780. https://doi.org/10.1109/23.819153 (1999).
14. Cheung, T., Butson, M. J. & Yu, P. K. N. Energy dependence corrections to mosfet dosimetric sensitivity. *Australasian Physics & Engineering Sciences in Medicine* **32**, 16–20. https://doi.org/10.1007/BF03178623 (2009).
15. di Franco, F. et al. Monocrystalline diamond detector for online monitoring during synchrotron microbeam radiotherapy. *Journal of Synchrotron Radiation* **30**, 1076–1085. https://doi.org/10.1107/S160057752300752X (2023).
16. Livingstone, J., Stevenson, A. W., Butler, D. J., Häusermann, D. & Adam, J.-F. Characterization of a synthetic single crystal diamond detector for dosimetry in spatially fractionated synchrotron x-ray fields. *Medical Physics* **43**, 4283–4293, https://doi.org/10.1118/1.4953833 (2016). https://aapm.onlinelibrary.wiley.com/doi/pdf/10.1118/1.4953833.
17. Archer, J. et al. X-ray microbeam measurements with a high resolution scintillator fibre-optic dosimeter. *Scientific Reports* **7**, 12450. https://doi.org/10.1038/s41598-017-12697-6 (2017).
18. Archer, J. et al. High spatial resolution scintillator dosimetry of synchrotron microbeams. *Scientific Reports* **9**, 6873. https://doi.org/10.1038/s41598-019-43349-6 (2019).
19. Ciarrocchi, E. et al. Oc-0932 plastic scintillator-based dosimeters for flash radiotherapy. *Radiotherapy and Oncology* (2023).
20. Khanarian, G. Optical properties of cyclic olefin copolymers. *Optical Engineering* **40**, 1024–1029. https://doi.org/10.1117/1.1369411 (2001).
21. Agha, A. et al. A review of cyclic olefin copolymer applications in microfluidics and microdevices. *Macromolecular Materials and Engineering* **307**, 2200053, https://doi.org/10.1002/mame.202200053 (2022). https://onlinelibrary.wiley.com/doi/pdf/10.1002/mame.202200053.
22. Zhang, Y., Gao, K. & Fan, Y. Application of a new uv curable adhesive for rapid bonding in thermoplastic-based microfluidics. *Micro & Nano Letters* **14**, 211–214, https://doi.org/10.1049/mnl.2018.5479 (2019). https://ietresearch.onlinelibrary.wiley.com/doi/pdf/10.1049/mnl.2018.5479.
23. Wu, W. et al. Noble metallic pyramidal substrate for surface-enhanced raman scattering detection of plasmid dna based on template stripping method. *Micromachines* **12**, https://doi.org/10.3390/mi12080923 (2021).
24. M.J. Berger, M. Z., J.S. Coursey & Chang, J. Nist standard reference database 124, https://doi.org/10.18434/T4NC7P (2017).
25. Fournier, P. et al. Absorbed dose-to-water protocol applied to synchrotron-generated x-rays at very high dose rates. *Physics in Medicine and Biology* **61**, N349–N361. https://doi.org/10.1088/0031-9155/61/14/N349 (2016).
26. Martínez-Rovira, I., Sempau, J. & Prezado, Y. Development and commissioning of a Monte Carlo photon beam model for the forthcoming clinical trials in microbeam radiation therapy: MC photon beam model for MRT clinical trials. *Medical Physics* **39**, 119–131. https://doi.org/10.1118/1.3665768 (2011).
27. Keshmiri, S. *Un système de planification de traitement multi-échelle pour la radiothérapie par micro faisceaux synchrotron - Validation expérimentale et dosimétrie biologique*. Ph.D. thesis (2023). Thèse de doctorat dirigée par Adam, Jean-François Physique de la matière condensée et du rayonnement Université Grenoble Alpes 2023.
28. Cornelius, I. et al. Benchmarking and validation of a Geant4-SHADOW Monte Carlo simulation for dose calculations in microbeam radiation therapy. *Journal of Synchrotron Radiation* **21**, 518–528. https://doi.org/10.1107/S1600577514004640 (2014).
29. Bräuer-Krisch, E. et al. The preclinical set-up at the id17 biomedical beamline to achieve high local dose deposition using interlaced microbeams. *Journal of Physics: Conference Series* **425**, 022001. https://doi.org/10.1088/1742-6596/425/2/022001 (2013).

30. Adam, J.-F. et al. Toward neuro-oncologic clinical trials of high-dose-rate synchrotron microbeam radiation therapy: First treatment of a spontaneous canine brain tumor. *International Journal of Radiation Oncology*Biology*Physics* **113**, 967–973, https://doi.org/10.1016/j.ijrobp.2022.04.022 (2022).
31. Ocadiz, A. et al. Film dosimetry studies for patient specific quality assurance in microbeam radiation therapy. *Physica Medica* **65**, 227–237. https://doi.org/10.1016/j.ejmp.2019.09.071 (2019).
32. Shi, Y., Ma, L., Zhuang, Y. & He, Z. Investigation on roughness-induced scattering loss of small-core polymer waveguides for single-mode optical interconnect applications. *Opt. Express* **28**, 38733–38744. https://doi.org/10.1364/OE.410283 (2020).
33. Ogilvie, I. R. G. et al. Reduction of surface roughness for optical quality microfluidic devices in pmma and coc. *Journal of Micromechanics and Microengineering* **20**, 065016. https://doi.org/10.1088/0960-1317/20/6/065016 (2010).
34. Leutz, H. Scintillating fibres. *Nuclear Instruments and Methods in Physics Research Section A: Accelerators, Spectrometers, Detectors and Associated Equipment* **364**, 422–448. https://doi.org/10.1016/0168-9002(95)00383-5 (1995).
35. Kharzheev, Y. N. Radiation hardness of scintillation detectors based on organic plastic scintillators and optical fibers. *Physics of Particles and Nuclei* **50**, 42–76. https://doi.org/10.1134/S1063779619010027 (2019).
36. Thevenet, F. et al. A heterogeneous-cavity model for miniaturized detectors of orthovoltage X-rays. *Journal of Physics: Conference Series* **2799**, 012012. https://doi.org/10.1088/1742-6596/2799/1/012012 (2024).
37. Keshmiri, S., Brocard, S., Serduc, R. & Adam, J.-F. A high-resolution dose calculation engine for x-ray microbeams radiation therapy. *Medical Physics* **49**, 3999–4017, https://doi.org/10.1002/mp.15637 (2022). https://aapm.onlinelibrary.wiley.com/doi/pdf/10.1002/mp.15637.
38. Li, Z. et al. Properties of plastic scintillators after irradiation. *Nuclear Instruments and Methods in Physics Research Section A: Accelerators, Spectrometers, Detectors and Associated Equipment* **552**, 449–455. https://doi.org/10.1016/j.nima.2005.06.075 (2005).
39. Papageorgakis, C. et al. Dose rate effects in radiation-induced changes to phenyl-based polymeric scintillators. *Nucl. Instrum. Meth. A* **1042**, 167445, https://doi.org/10.1016/j.nima.2022.167445 (2022). arXiv:2203.15923.
40. Secerov, B., Marinović-Cincović, M., Popovic, S., Nedić, Z. & Kačarević-Popović, Z. Characterization of gamma irradiated ethylene-norbornene copolymer using ftir, uv-vis and dsc techniques. *Polymer Bulletin* **60**, https://doi.org/10.1007/s00289-007-0867-5 (2008).
41. Durante, M., Bräuer-Krisch, E. & Hill, M. Faster and safer? FLASH ultra-high dose rate in radiotherapy. *The British Journal of Radiology* **91**, 20170628, https://doi.org/10.1259/bjr.20170628 (2018). Publisher: The British Institute of Radiology.
42. Prezado, Y., Martínez-Rovira, I. & Sánchez, M. Scatter factors assessment in microbeam radiation therapy. *Medical Physics* **39**, 1234–1238, https://doi.org/10.1118/1.3681274 (2012). _eprint: https://onlinelibrary.wiley.com/doi/pdf/10.1118/1.3681274.
43. Reynard, D. & Hugtenburg, R. P. A Monte Carlo intercomparison of peak-to-valley dose ratios and output factors for microbeam radiation therapy. *Radiation Physics and Chemistry* **176**, 108980. https://doi.org/10.1016/j.radphyschem.2020.108980 (2020).

Acknowledgements

We acknowledge the European Synchrotron Radiation Facility (ESRF) for provision of synchrotron radiation facilities and we would like to thank Paolo Pellicioli and Herwig Requardt for assistance and support in using beamline ID17. This work was performed within the framework of the LABEX PRIMES (ANR-11-LABX-0063) of Université de Lyon, within the program "Investissements d'Avenir" operated by the French National Research Agency (ANR). FT, SK, JFA and PP were financially supported by ITMO Cancer of Aviesan within the framework of the 2021-2030 Cancer Control Strategy, on funds administered by INSERM (INCA - PCSI / 2023 / IODA-Master / 23CP088-00 / ADAM). The authors personally thank Paolo Pellicioli for his support, the fruitful discussions and the spectral data that is implemented in SK's simulations. This work was supported by Nanolyon platform, a member of the CNRS-RENATECH+ French national network. We would also like to express our gratitude to the NanoLyon platform affiliated individuals who contributed to various stages, particularly Nicolas Terrier and Magalie Faivre. We also thank our research engineer Missipssa Moussaoui for his contribution during the cleanroom development.

Author contributions

S.K. participated in the ESRF experiments and contributed to the Monte Carlo simulations, J.D. contributed to the creation of the synchrotron setup, P.P. was involved in the concept and realization, J.A. participated in the synchrotron experiments and the medical physics aspect of the project, G.L. contributed to UV-testing data analysis, J.L. contributed to Synchrotron testing data analysis and F.T. was involved in every stage of development and experimentation. All authors contributed to the review of this article.

Declarations

Competing interests

The authors declare no competing interests.

Additional information

Correspondence and requests for materials should be addressed to P.P.

Reprints and permissions information is available at www.nature.com/reprints.

Publisher's note Springer Nature remains neutral with regard to jurisdictional claims in published maps and institutional affiliations.

Open Access This article is licensed under a Creative Commons Attribution-NonCommercial-NoDerivatives 4.0 International License, which permits any non-commercial use, sharing, distribution and reproduction in any medium or format, as long as you give appropriate credit to the original author(s) and the source, provide a link to the Creative Commons licence, and indicate if you modified the licensed material. You do not have permission under this licence to share adapted material derived from this article or parts of it. The images or other third party material in this article are included in the article's Creative Commons licence, unless indicated otherwise in a credit line to the material. If material is not included in the article's Creative Commons licence and your intended use is not permitted by statutory regulation or exceeds the permitted use, you will need to obtain permission directly from the copyright holder. To view a copy of this licence, visit http://creativecommons.org/licenses/by-nc-nd/4.0/.

© The Author(s) 2024